BIOCHEMISTRY
including biophysical chemistry & molecular biology

ARTICLE

pubs.acs.org/biochemistry

Dynamics of a Heparin-Binding Domain of $VEGF_{165}$ Complexed with Its Inhibitor Triamterene

Ki-Woong Jeong,[†] Jee-Young Lee,[†] Sung-Ah Lee,[†] Seung-Pil Yang,[§] Hyunsook Ko,[†] Dong-Il Kang,[‡] Chi-Bom Chae,[§] and Yangmee Kim*[,†]

[†]Department of Bioscience and Biotechnology and Bio/Molecular Informatics Center, Konkuk University, Seoul 143-701, Korea

[‡]Department of Chemistry, Konkuk University, Seoul 143-701, Korea

[§]Institute of Biomedical Science and Technology, Konkuk University, Seoul 143-701, Korea

ABSTRACT: Vascular endothelial growth factor (VEGF), which has neurotrophic and neuroprotective effects in addition to its major role in angiogenesis, interacts with Aβ and accumulates in the senile plaques of Alzheimer's disease (AD) patients' brains. It is known that Aβ binds to the heparin-binding domain (HBD) of the 165-amino acid VEGF variant, $VEGF_{165}$. In this study, we showed that triamterene (Trm) inhibits VEGF−Aβ interaction without affecting other biological activities of VEGF or Aβ. We investigated the importance of structural and dynamic features of HBD for its molecular-recognition processes. The binding model of HBD and Trm was constructed based on measurements of chemical shift changes and docking study. The results showed that the loop region (S11−L17) and F18 at the beginning of the first β-sheet in the HBD constitute the inhibitor binding site. The N1 atom of pteridine ring of Trm forms hydrogen bonding with backbone amide proton of R13, and the phenyl ring took part in a hydrophobic interaction with the aromatic ring of F18. To investigate the functional importance of the inherent structural flexibility of the HBD in VEGF, the dynamic properties of free HBD and HBD−Trm complex were assessed by measuring spin relaxation rates, and the backbone dynamics were investigated by model-free analysis. The residues in the disordered loop region of the N-terminus exhibited conformational exchanges in free HBD, and flexibility of this loop region decreased dramatically upon binding to Trm, suggesting that Aβ as well as inhibitor may recognize these unique dynamic features of the HBD. Furthermore, C-terminal residues continued to exhibit slow conformational motions, even in the HBD−Trm complex, implying that these motions at the C-terminus of the HBD might be important for interactions with heparin molecules. The flexibility of HBD demonstrated here should be essential for VEGF function and interaction with other protein partners.

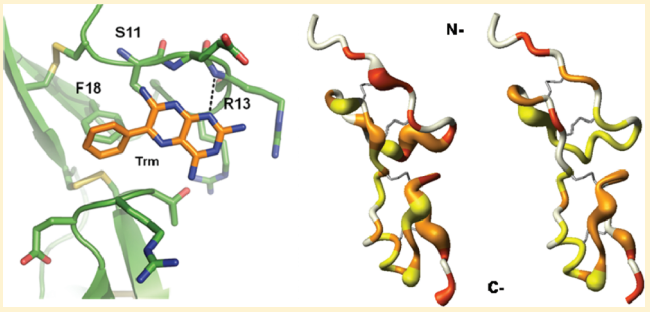

β-Amyloid (Aβ) is major component of the senile plaques that are deposited in the brains of patients with Alzheimer's disease (AD), the most common form of dementia among the elderly.[1−3] We previously reported that vascular endothelial growth factor (VEGF) interacts with Aβ with specificity and high affinity and thereby co-accumulates with Aβ in the senile plaques of the AD brain.[4] Specially, Aβ binds the 55-residue C-terminal domain of the 165-amino acid (aa) VEGF variant, $VEGF_{165}$.[5]

VEGF is a key regulator of pathological angiogenesis, which is involved in cancer, rheumatoid arthritis, and retinopathy.[6−10] In addition, VEGF has neurotropic as well as neuroprotective functions.[11−13] The active form of VEGF is a 41−46 kDa homodimer linked by two disulfide bridges. The overall structure of the VEGF monomer has been previously reported to consist of a central antiparallel four-stranded β-sheet containing a cysteine knot motif at one end.[14−18] There are four variants of VEGF—$VEGF_{121}$, $VEGF_{165}$, $VEGF_{189}$, and $VEGF_{206}$—produced from a single gene through alternative splicing; all subtypes have six C-terminal residues and share the same 115-aa N-terminus, which includes the binding sites for VEGF receptors.[19,20] VEGF variants are variably expressed in different tissues, but all mediate mitogenic actions and regulate vascular permeability in endothelial cells and are the main regulators of hypoxia and tumor-induced angiogenesis. One of the most abundant isoforms, $VEGF_{165}$, binds heparin through a C-terminal, 55-aa-residue heparin-binding domain (HBD).[21]

Heparin binding is important for the stability of VEGF;[22] it enhances the mitogenic activity of $VEGF_{165}$, and it is essential for binding of $VEGF_{165}$ to the VEGF receptor.[23,24] The HBD is divided into two domains: an N-terminal subdomain (residues 1−29) containing the interface loop region (residues 11−17) and a C-terminal subdomain (residues 29−55).[25] The HBD of VEGF is structurally unique compared with that of other known heparin-binding proteins.[6,22] It is highly basic, with an estimated pI of ∼11.3, and contains eight cysteine residues that form four

Received: January 18, 2011
Revised: May 5, 2011
Published: May 05, 2011

disulfide bonds. The structure of the VEGF HBD has been solved by nuclear magnetic resonance (NMR) spectroscopy.[25,26] The N-terminal region, containing two disulfide bonds (C7−C25 and C10−C27), is composed of a disordered region from S11 to L17 and a single two-stranded antiparallel β-sheet structure encompassing F18 to D21 and K26 to C29.[25] The C-terminal region, which also has two disulfide bonds (C29−C48 and C36−C50), is well ordered and contains a short α-helix from D33 to A38 packed against a two-stranded antiparallel β-sheet structure consisting of E42 to N44 and R49 to D51.[25]

We have proposed that the accumulation of VEGF on senile plaques would induce local VEGF deficiency that might contribute to neuronal and cerebrovascular degeneration.[4] Therefore, it will be important to prevent precipitation of VEGF through the binding with amyloid plaques. We previously screened various synthetic and natural compounds for materials that inhibit VEGF−Aβ interactions and potentially alleviate local VEGF deficiencies. These studies identified triamterene (Trm) as an inhibitor of interaction between VEGF and Aβ with a moderate activity (IC_{50} of 50 μM).[27] However, Trm has the desired quality, that is, inhibition of binding of VEGF with Aβ without affecting the activity of VEGF. This could be advantageous for treatment of Alzheimer's disease since VEGF has neurotropic as well as neuroprotection functions in addition to the maintenance of healthy blood vessels in the brain. Trm is a well-known potassium-sparing diuretic that is widely used for the treatment of edema and hypertension.[28] We discovered that Trm binds to the HBD domain of VEGF. Therefore, investigation of the interaction between HBD and Trm may provide important information for the development of more potent inhibitors of VEGF−Aβ interaction which can be used as a therapeutic agent for Alzheimer's disease.

Flexibilities in protein conformation are essential for enzymatic function, playing key roles in molecular recognition, rate-limiting conformational transitions, and catalysis.[29−32] The time scales of these protein conformational motions are widely distributed from picoseconds to seconds, making solution NMR a suitable technique for analyzing such motions. Here, in order to understand the importance of structural and dynamic features of HBD for its molecular-recognition processes, we proposed a binding model of Trm and HBD based on chemical shift perturbations and analyzed the dynamic properties of free HBD and HBD−inhibitor complex using NMR spin-relaxation techniques. The results showed that the inherent structural flexibilities of the N-terminal loop region of HBD are important in inhibitor-recognition process as well as for the binding of Aβ to VEGF, and this result may provide insight into the development of more potent inhibitor.

2. MATERIALS AND METHODS

2.1. Binding Assays. Human recombinant $VEGF_{165}$ was produced in *Escherichia coli* and purified as described previously.[33] Briefly, refolded $VEGF_{165}$ was purified by Mono-S cation exchange column chromatography (Amersham Pharmacia Biotech, Arlington Heights, IL) and further purified on a C4 reverse-phase HPLC column (Phenomenex, Torrance, CA).[33] $A\beta_{1-42}$, purchased from American Peptide Co. (Sunnyvale, CA), was dissolved in sterile, deionized, distilled water at a concentration of 1 mg/mL (stock solution) and stored at −70 °C.[5] The entire ectodomain of KDR (kinase insert domain receptor) fused with the Fc fragment of human IgG1 was cloned into a baculoviral expression vector and purified by metal-affinity chromatography, as previously described.[34]

$VEGF_{165}$ was immobilized on plastic microtiter wells at a concentration of 10 nM, and nonspecific sites were blocked with 3% bovine serum albumin in phosphate-buffered saline (PBS) containing 0.1% Tween-20. For VEGF−Aβ binding assays, biotinyl-$A\beta_{1-42}$ (20 nM), alone or in the presence of different concentrations of Trm, were added to the wells and incubated for 3 h. After removing unbound biotinyl-$A\beta_{1-42}$, the bound $A\beta_{1-42}$ was determined using horseradish peroxidase (HRP)-conjugated streptavidin. For VEGF-KDR-Fc binding assays, KDR-Fc, together with Trm or epigallocatechin gallate (EGCG; positive control), was added to the wells with immobilized VEGF and incubated for 3 h. The VEGF-bound KDR-Fc was determined by incubating with a rabbit anti-Fc antibody followed by incubation with an HRP-conjugated anti-rabbit antibody.

2.2. Cytotoxicity Assays. Rat pheochromocytoma (PC12) cells were grown on poly(D-lysine)-coated dishes in RPMI 1640 containing 10% horse serum, 5% fetal bovine serum, and 1% antibiotics. Cells were seeded in poly(D-lysine)-coated 96-well plates at 2×10^4 cells/well. Different concentrations of Trm were then added to the cells in the presence of $A\beta_{1-42}$ and incubated for 24 h. The effect of Trm on Aβ cytotoxicity was determined using an ethidium homodimer-1-based LIVE/DEAD assay (Molecular Probes, Eugene, OR), as described by the manufacturer. The value obtained for the cells treated with PBS was subtracted from that of treated cells; 100% cell death was defined as the value obtained after treatment with 70% MeOH for 30 min.

2.3. Aβ Aggregation Assay. The effect of Trm on the aggregation of $A\beta_{1-42}$ was determined using a thioflavin T (ThT) assay, as described previously.[35] Briefly, $A\beta_{1-42}$ was diluted with PBS to 50 μM in the presence of different concentrations of Trm and incubated at 37 °C for 1 day. At the end of the incubation, 10 μM ThT in 5 mM phosphate buffer (pH 7.4) containing 150 mM NaCl was added to the aggregation mixture. Thereafter, fluorescence was measured at excitation and emission wavelengths of 444 and 485 nm, respectively, using a GeminiEM microplate fluorescence reader (Molecular Devices, Sunnyvale, CA).

2.4. Determination of Reactive Oxygen Species. The effect of Trm on the reactive oxygen species (ROS)-generating activity of Aβ was determined using a fluorescence assay. In this assay, the oxidant-sensitive fluorescent probe 2′,7′-dichlorofluorescein−diacetate (DCF-DA) was added at a final concentration of 20 μM directly to PC12 cells grown on 35 mm dishes and incubated for 1 h at 37 °C. Then, Aβ (5 μM) was added along with different concentrations of Trm and incubated for 12 h. After rinsing cells with serum-free medium, fluorescence was measured with a confocal microscope (Carl Zeiss, Weimar, Germany) at excitation and emission wavelengths of 485 and 538 nm, respectively.

2.5. Expression and Purification of the HBD. VEGF cDNA was previously cloned[33] into a pRSET-A vector (Invitrogen, Carlsbad, CA) containing a T7 promoter and an ampicillin-resistance cassette. ^{15}N-labeled HBD was produced from the *E. coli* transformed by the recombinant plasmid in 1 L of M9 minimal media supplemented with ampicillin and 1 g/L $^{15}NH_4Cl$ (Cambridge Isotope Laboratories, Cambridge, MA). The HBD was purified according to a previously published method.[25] Correctly folded, His-tagged HBD was purified by affinity chromatography using a HiTrap chelating column. The His-tag was removed from HBD by cleavage with enterokinase (Invitrogen, Carlsbad, CA), and final purification was achieved by cation

exchange chromatography using a HiTrap SP FF column (GE Healthcare, Uppsala, Sweden) eluted with a 0−1 M NaCl gradient. Samples for NMR were resuspended in 25 mM sodium d_3-acetate buffer (pH 5.5) containing 0.02% NaN_3.

2.6. Circular Dichroism Measurements of the HBD. Circular dichroism (CD) experiments were performed using a J810 spectropolarimeter (Jasco, Tokyo, Japan) with a 1 mm pathlength cell. The CD spectra of free HBD and HBD complexed with Trm in 25 mM sodium acetate buffer (pH 5.5) at 27 °C were recorded at 0.1 nm intervals from 190 to 250 nm. The peptide concentration was 20 μM for all CD experiments. For each spectrum, the data from 10 scans were averaged and smoothed using J810 software. CD data were expressed as the mean residue ellipticity $[\theta]$ in deg cm^2 dmol^{-1}.

2.7. Analysis of Trm−HBD Binding Using ^{15}N−^{1}H Heteronuclear Single-Quantum Coherence Spectra. ^{15}N-labeled HBD in sodium acetate buffer were 0.4 mM solutions in 0.3 mL of 9:1 (v/v) H_2O/D_2O (pH 5.5) for heteronuclear single-quantum coherence (HSQC) analysis. The Trm stock solution was prepared in DMSO-d_6. Chemical shift changes in the ^{1}H−^{15}N spectra of the HBD were obtained by titration with Trm. The magnitude of the chemical shift perturbation and changes in the intensities upon binding Trm were utilized to map binding site residues in the HBD. 2D NMR titration experiments were conducted in which Trm was added with various protein/Trm ratios (1:0−1:10). All NMR experiments were performed at 300 K on a Bruker Advance 500 MHz spectrometer at the Korea Basic Science Institute (KBSI).

2.8. Docking Study. A molecular docking study and molecular dynamic (MD) simulations were conducted to construct a binding model of Trm and HBD. The docking program AutoDock 3.05 was used to find the initial configurations for Trm and HBD complex structures. All HBD atoms were fixed, with the exception of those in a segment of the N-terminal loop region from S11 to F18. Residues from S11 to R13, and F18, were unrestrained, whereas residual residues in the N-terminal loop region from S11 to F18 were fixed, but the side-chain conformations and orientations remained unrestrained. To deduce the extent of motion and the errors associated with our estimates, we applied simple distance constraints (2.2−3.5 Å) between the N1 and N2 of Trm and the backbone nitrogen of R13 in all calculations. AutoDock calculates the ligand−protein interaction energies over a grid that encompasses the binding site of the protein and uses the Lamarckian genetic algorithm to search the protein−ligand complex with free-energy minimization.[36,37] A distance-dependent function of the dielectric constant was used to calculate energetic maps; default values were used for all other parameters. MD simulations, performed in the canonical ensemble (NVT) at 300 K using the program InsightII/Discover (Accelrys Inc., San Diego, CA), were carried out using the final docking structures. All atoms of the system were considered explicitly, and their interactions were computed using the force field analysis package, CHARMM. A distance cutoff of 10 Å was used for van der Waals interactions and electrostatic interactions. The time step in the MD simulations was 1 fs; MD simulations were performed for 5 ns. Coordinates were saved every 2 ps.

2.9. Investigation of Backbone Dynamics by NMR. NMR studies utilized the resonance assignments of the HBD reported previously by Fairbrother et al.[25] Ambiguities in resonance assignments of Trm-bound HBD were resolved by recording ^{15}N-edited NOESY-HSQC[38] and ^{15}N-edited TOCSY-HSQC.[39] NMR spin-relaxation experiments were performed using previously published gradient-selected, sensitivity-enhanced pulse sequences.[40−42] The longitudinal (R_1) spin-relaxation rates were measured with relaxation delays of 0.002 (×2), 0.045, 0.1, 0.2, 0.315 (×2), 0.55, 0.8, and 1.0 s. The transverse (R_2) relaxation rates were obtained with total relaxation delays of 0.0 (×2), 0.0176, 0.0352, 0.0528 (×2), 0.068, 0.1145, 0.184, and 0.284 s. For R_2 measurements, temperature-compensating ^{15}N 180° pulses were applied during the recycle delay.[43] The heteronuclear cross-relaxation rate was obtained from nuclear Overhauser effect (NOE) experiments by interleaving pulse sequences with and without proton saturation. The recycle delay and proton saturation time in the heteronuclear NOE measurement were 4.5 and 3.0 s, respectively. All relaxation spectra were acquired with the ^{1}H carrier set coincident with the water resonance and ^{15}N frequency set to 118 ppm; spectral widths were 5498 and 1612 Hz in the t_2 and t_1 dimensions, respectively, with 2048 and 200 complex points in each dimension. A recycle delay of 2.5 s was used in all R_1 and R_2 relaxation experiments. NMR data were processed with NMRPipe[44] and visualized with Sparky.[45] Typically, 35.0 μs ^{15}N 90° pulse widths were achievable with an *xyz*-gradient-equipped Bruker TXI (^{1}H, ^{13}C, ^{15}N) probe.

The heteronuclear NOE was determined from the ratio of peak heights for experiments with and without proton-saturation pulses. R_1 and R_2 rates were determined by fitting the peak heights using the program Curvefit available at the Palmer group's homepage (http://biochemistry.hs.columbia.edu/labs/palmer/software/curvefit.html).

2.10. Model-Free Analysis. Protein amide backbone dynamics were characterized by fitting NMR spin-relaxation rates to one of five semiempirical forms of the spectral-density function using model-free formalism.[46,47] The five models used to describe the spin-relaxation data are described according to their corresponding parameters, as previously published.[48] Briefly, the five models considered were (1) S^2 only; (2) S^2 and τ_e; (3) S^2 and R_{ex}; (4) model 2 plus R_{ex}; and (5) S_f^2, S^2, and τ_e, the extended two-time scale model.[48,49] Here, τ_e is the internal correlation time; S^2 is the generalized order parameter; S_f^2 is the order parameter for fast motion, with typical correlation time <10 ps; and R_{ex} is the additional line broadening due to assumed two-site conformational exchange and depends on the equilibrium site populations, the chemical shift differences, and the rate of exchange between conformers. Motional parameters were fitted to the spin-relaxation data using the selection method described for the program FAST-Model-free developed by Loria and colleagues[48] interfaced with Model-Free 4.16.[50] Model selection was based on the statistical testing protocol described previously by Mandel et al.[51] The programs pdbinertia and R2R1 Diffusion were downloaded from the homepage of Palmer's group (http://biochemistry.hs.columbia.edu/labs/palmer/software/diffusion.html) for calculating the inertia tensor from PDB coordinates of the HBD (1KMX[26]) and final docking structure of HBD complexed with Trm and diffusion tensor from ^{15}N R_2/R_1 experimental relaxation data. The criteria for inclusion of residues in the diffusion tensor estimate relied on the method of Tjandra et al.[52] Since R_2 values are loaded with R_{ex} contributions and most of the microsecond−millisecond exchange in HBD were caused mainly by due to disulfide isomerization, the data containing R_{ex} were not included in calculation for calculation of the diffusion tensor and correlation time.

During the model-free analysis, an axially symmetric rotational diffusion tensor was used, the N−H bond lengths were assumed to be 1.02 Å, and the ^{15}N chemical shift anisotropy

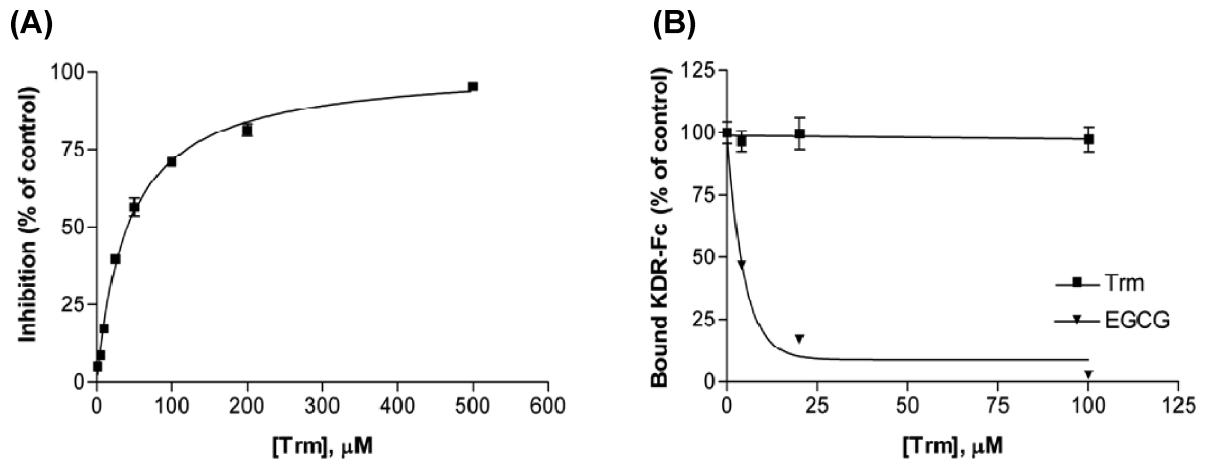

Figure 1. Inhibitory effects of Trm (A) on the binding of Aβ to VEGF and (B) on VEGF-VEGFR (KDR) interactions. For VEGF−Aβ binding assays, biotinyl−Aβ_{1-42} (20 nM), alone or in the presence of different concentrations of Trm, were added to wells containing immobilized $VEGF_{165}$. For VEGF-KDR-Fc binding assays, KDR-Fc, together with Trm or epigallocatechin gallate (EGCG; positive control), was added to the wells with immobilized $VEGF_{165}$.

was assumed to be −160 ppm.[53,54] For each model, 300 randomly distributed data sets were generated. Models were selected by comparing the sum-squared error of the optimal fit with the 0.05 critical value of the distribution. In cases where *F*-statistics were applicable, comparisons were made with the 0.20 critical value of the distribution.

3. RESULTS

3.1. Differential Effects of Trm on the Interactions of VEGF with Aβ and the VEGF Receptor, KDR. To investigate the inhibitory effect of Trm on Aβ binding to VEGF, we used an avidin−biotin-based microplate assay employing $VEGF_{165}$ immobilized on 96-well plates. Biotinyl-Aβ_{1-42} (20 nM), alone or in the presence of different concentrations of Trm, was added to wells containing immobilized $VEGF_{165}$; binding was determined by monitoring the activity of HRP-conjugated streptavidin. As shown in Figure 1A, Trm inhibited the binding of Aβ to VEGF with an IC_{50} of 50 μM.

We then investigated the effect of Trm on the interaction of VEGF with KDR, a cell surface receptor for VEGF that transduces intracellular VEGF signals. In the KDR-VEGF binding assay, Trm at concentrations up to 100 μM did not inhibit KDR binding to VEGF. In contrast, EGCG, a known inhibitor of VEGF,[55,56] induced a dose-dependent inhibition of VEGF-KDR binding, and completely abrogated binding at 100 μM (Figure 1B).

3.2. Absence of an Effect of Trm on Aβ Aggregation, Cytotoxicity, and ROS-Generating Activity. Because Trm was found to inhibit VEGF−Aβ interaction, we investigated the characteristics of Trm in greater detail, focusing on the effects of Trm on Aβ aggregation and ROS generation—well-known mechanisms underlying the cytotoxicity of Aβ. Aβ alone induced ~75% cell death, as measured in a LIVE/DEAD assay. Trm had no effect on Aβ cytotoxicity (Figure 2A) and was not cytotoxic to cells at concentrations below 50 μM. An investigation of the effects of Trm on Aβ aggregation and Aβ-induced ROS generation, which are closely related to its toxicity, showed that Aβ alone readily formed aggregates and generated ROS. However, the addition of Trm had no effect on either phenomenon, as shown in Figure 2B,C. Trm alone did not generate ROS, as shown in Figure 2C.

3.3. CD Measurements of the HBD. We next investigated the secondary structures of free HBD and HBD complexed with Trm by analyzing their CD spectra, as shown in Figure 3A. The CD spectrum of free HBD showed a negative band at approximately 195−200 nm, indicating that the HBD does not have stable secondary structures. As shown in Figure 3B, the tertiary folding of the HBD might be maintained by four disulfide bonds (C7−C25, C10−C27, C29−C48, and C36−C50) present in this domain. HBD complexed with Trm showed shift in CD spectra around 210 nm, which is characteristic of a β-sheet structure. These results imply that complexation with Trm stabilizes the secondary structure of the HBD.

3.4. Chemical Shift Perturbations of the HBD upon Trm Binding. Chemical shift perturbations of a protein can be caused by local structural rearrangements that occur upon binding a ligand. To assess the effects of Trm binding, we performed Trm titration experiments and analyzed the backbone ^{15}N and ^{1}HN chemical shift variations by comparing the $^{1}H-^{15}N$ HSQC spectrum of free HBD with that of HBD in presence of Trm. In the case of both free and Trm-bound HBD, nonproline backbone residues except E12 and R54 could be assigned without overlapping. Overlay of the $^{1}H-^{15}N$ HSQC spectra of free HBD and Trm-complexed HBD (a molar ratio of HBD to Trm of 1:5) is shown in Figure 4A, and the chemical shift perturbations calculated by the method of Wuthrich and co-workers[57] are depicted in Figure 4B. When we analyzed the NMR signals of 0.4 mM HBD while titrating Trm at ratios of 0:1, 1:1, 2:1, 5:1, and 10:1 concentration of Trm with respect to HBD, peaks in N-terminal loop region showed big chemical shift perturbations. In Figure 4B, changes in chemical shift upon binding with Trm are indicated by open bars. Large chemical shift perturbations (>0.1 ppm) indicated by black bar were observed for S11, R13, L17, and F18 residues. In the case of R14 and K15, there were very little change in chemical shift upon binding Trm. Peaks of S11, R13, R14, and H16 in HSQC spectra of HBD completely disappeared with addition of Trm at the ratio of 10:1 of Trm with respect to HBD. Notably, the NH peak of L17 and F18 remained at this ratio. Figure 4C shows the peak traces of S11, L17, F18, and L41 for the Trm titration in $^{1}H-^{15}N$ HSQC. The NH peak of L41 as a control did not show any changes in chemical shift with Trm while NH peak of S11, L17, and F18 showed large

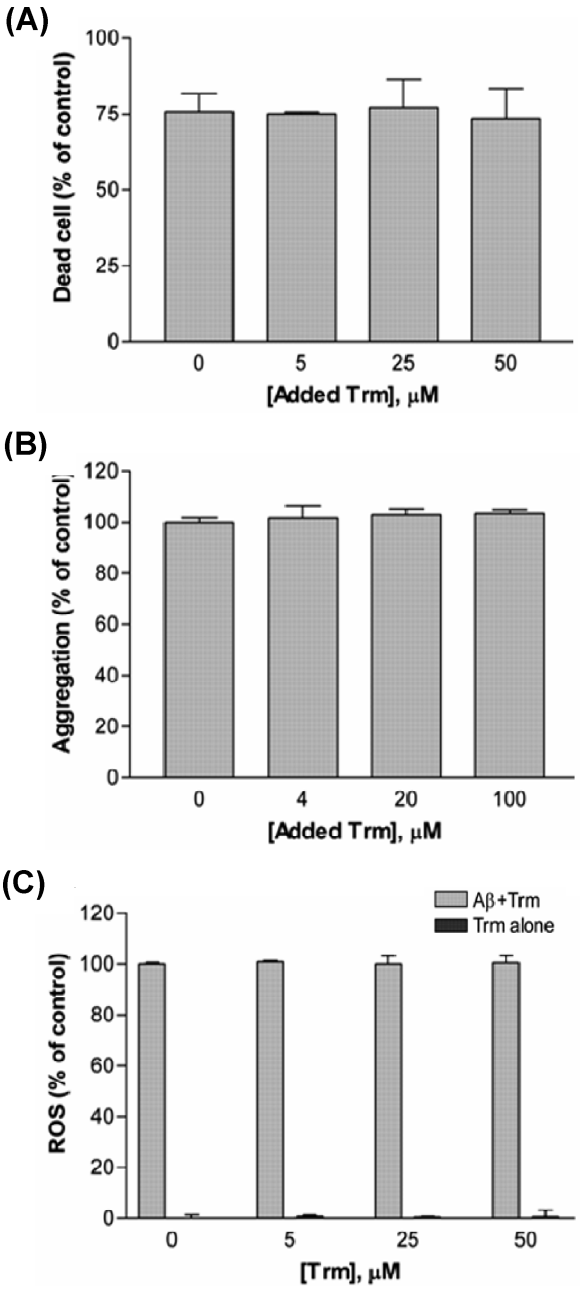

Figure 2. Trm effects on Aβ aggregation and Aβ-mediated toxicity and ROS generation. Trm has no effect on Aβ toxicity (A), aggregation (B), or ROS-generating activity (C).

chemical shift perturbations. Chemical shift perturbation arose through fast exchange upon weak binding of Trm to the HBD, concluding that residues in N-terminal loop region from S11 to F18 of the HBD constitute the Trm binding site.

3.5. Solution-NMR Experiments. We then compared the dynamic properties of HBD and HBD complexed with Trm. The results of spin-relaxation experiments with free HBD and Trm-bound HBD (a molar ratio of HBD to Trm of 1:5) are compared in Figure 5. Because of spectral overlap of resonance of E12 and R54 in $^{1}H-^{15}N$ HSQC spectra, we could not obtain the relaxation rate parameters for E12 at the Trm binding site. The average (10% trimmed) R_1, R_2, and NOE values of free HBD were 2.41 $\pm$ 0.023, 7.17 $\pm$ 0.13, and 0.61 $\pm$ 0.010 s^{-1}, respectively, whereas the

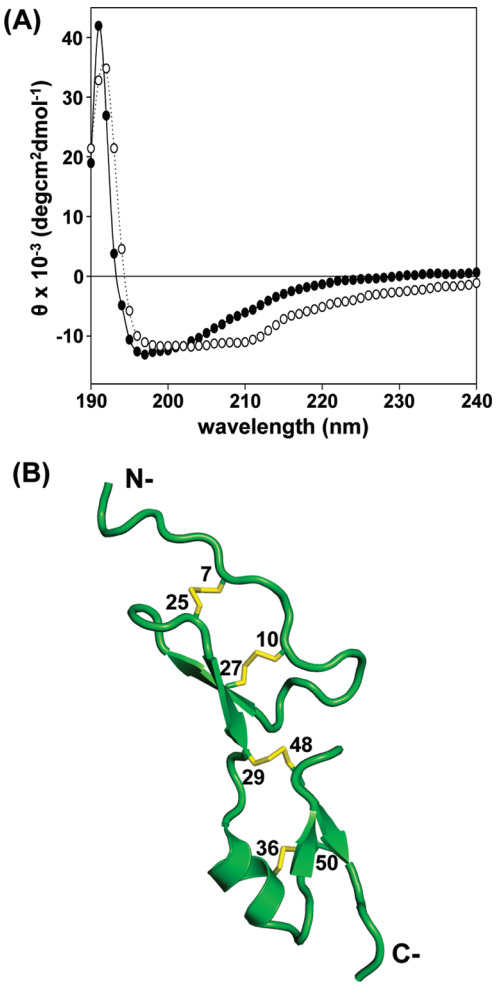

Figure 3. (A) CD spectra of free HBD (filled circles) and HBD complexed with Trm (open circles) in 25 mM sodium acetate (pH 5.5) at 300 K. (B) Ribbon structure of HBD showing secondary structural elements and four disulfide bonds in yellow.

corresponding values of bound HBD were 2.49 $\pm$ 0.074, 7.33 $\pm$ 0.25, and 0.67 $\pm$ 0.016 s^{-1}. The average R_2/R_1 ratio for free HBD was determined to be 2.98 $\pm$ 0.13, whereas that for bound HBD was 2.94 $\pm$ 0.26, implying that the HBD always exists in a monomeric form. Large R_2 values (>10 s^{-1}) were observed for the backbone N−H of S11, R13, H16, D21, C25, C27, S34, Q40, N44, C48, C50, and D51 in the HBD spin-relaxation rate data. These residues are distributed in the N-terminal disordered loop region, the loop region between the short helix and the β-sheet, and regions near proline residues or disulfide bonds. These large R_2 values could be due to large contributions from conformational exchange (R_{ex}) of the protein on the micro- to millisecond time scale. In the Trm binding loop region from S11 to F18, R_2 values of S11 and R13 were decreased more than 5.0 s^{-1} upon binding to Trm while R_2 values of R14, H16, and L17 were increased more than 2.0 s^{-1} upon binding to Trm. From this, we conclude that conformational exchange of S11 and R13 was reduced upon binding to Trm. However, R_2 values of some C-terminal subdomain residues in the 30−55 region, namely S34, Q40, N44, C48, and C50, were increased by more than 2.0 s^{-1} upon binding of Trm.

The residues at both termini in free HBD and Trm-bound HBD have very low heteronuclear NOE values because of flexibility. In free HBD, the residues in the N-terminal loop

dx.doi.org/10.1021/bi2000752 |*Biochemistry* 2011, 50, 4843–4854

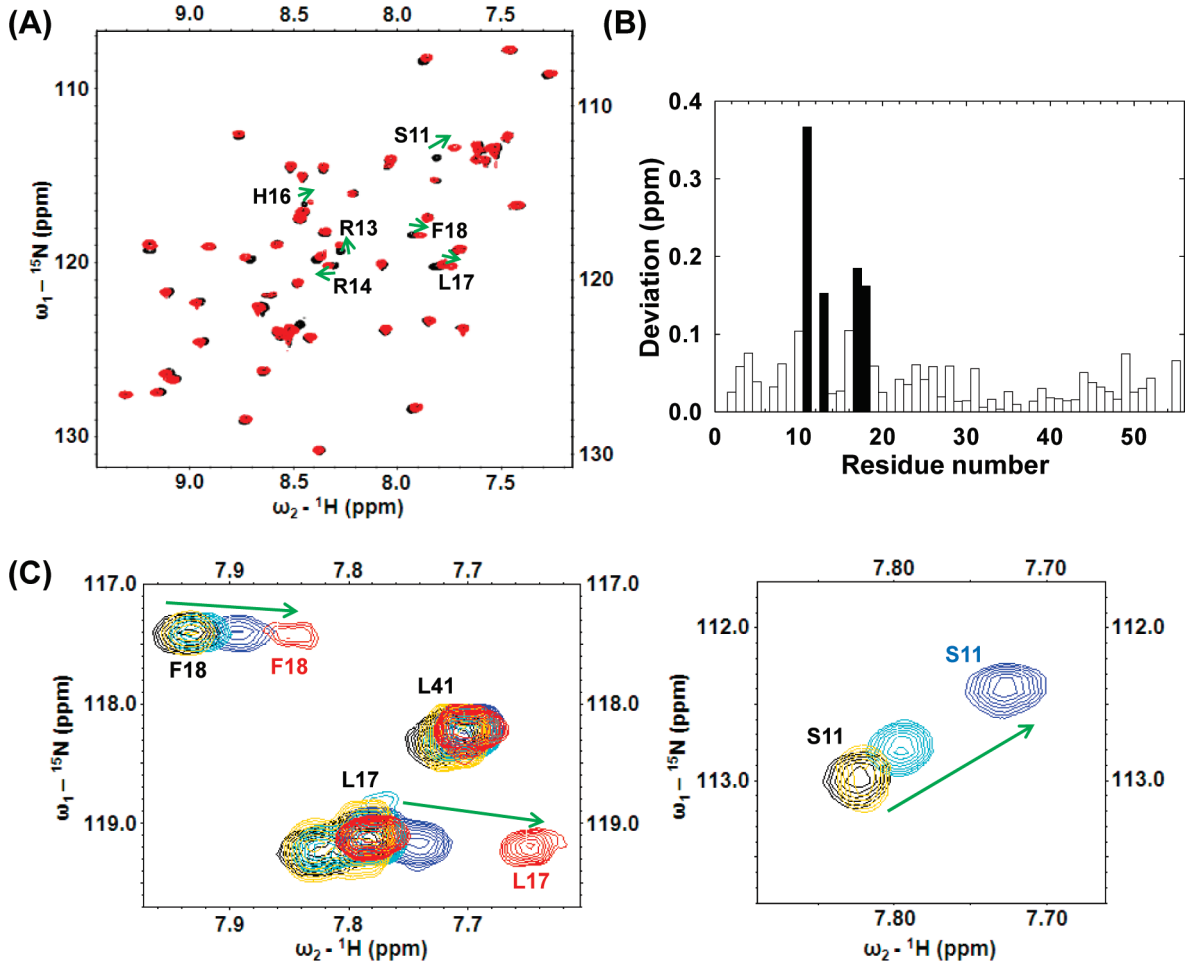

Figure 4. (A) Overlay of HSQC spectra of free HBD in black and Trm-bound HBD in red (a molar ratio of HBD to Trm of 1:5). (B) Chemical shift perturbations ($\Delta\delta = [\delta H^2 + 0.2(\delta^{15}N)^2]^{1/2}$) of 0.4 mM HBD at a molar ratio of HBD to Trm of 1:10.[57] Perturbation of S11, R13, R14, and H16 were plotted at a molar ratio of HBD to Trm of 1:5 because peaks of these residues were disappeared in the HSQC spectra at a molar ratio of HBD to Trm of 1:10. (C) Peak traces for the Trm titration in ^{1}H−^{15}N HSQC spectra. 2D spectra show the signal changes of 0.4 mM HBD while titrating Trm at ratios of (a) 0:1 (black), (b) 1:1 (yellow), (c) 2:1 (sky blue), (d) 5:1 (blue), and (e) 10:1 concentration of Trm with respect to HBD (red). Shifting path of the peaks is indicated by the arrows.

region showed much lower NOE values compared to the other residues. Notably, binding of Trm to the HBD increased the NOE values of the residues near the N-terminal loop region, including the residues from S11 to F18 because of stabilization of the HBD structure upon binding of Trm. However, heteronuclear NOE values of C-terminal subdomain residues in the 30−55 region did not change much upon binding of Trm. Interestingly, most NOE values of the side-chain amides of glutamine and asparagines were negative because of their flexibility; however, the side-chain amide of Q20 and N44 showed positive heteronuclear NOE values (Figure 6). Tertiary structure determined by NMR spectroscopy revealed hydrogen bonding between side-chain carbonyls of N44 and backbone NH of R46 and between the side chain of Q20 and the carbonyl oxygen of G8.[25] Also, it was indicated that the side chain of Q20 participates in hydrophobic interactions with both disulfide bridges, C7−C25 and C10−C27.[25] Therefore, the side-chain amide protons of Q20 and N44 have high structural rigidity compared to the side chains of other glutamines and asparagines, resulting in abnormally high NOE values.

The average value of heteronuclear NOE at the Trm-binding region from S11 to F18 was 0.593 ± 0.014 for free HBD and was dramatically increased to 0.753 ± 0.034 for the Trm-bound form of the HBD. These results imply that Trm binds to the N-terminal loop region of HBD, which becomes more rigid upon ligand binding, and are consistent with the results of CD measurements indicating increased stability of the secondary structure of the HBD−Trm complex.

3.6. Binding Model of Trm and HBD Constructed Based on Docking Study Results. Using the NMR data, we constructed a possible model of the binding of Trm and HBD. The 3D structure of Trm, with a numbering scheme, is presented in Figure 7A. Upon binding of Trm, peaks of three HBD residues in the N-terminal loop region—S11, R13, and F18—exhibited large chemical shift perturbations as well as increase of hererononuclear NOE and decrease of conformational exchange as shown in Figures 4 and 5. The chemical shift perturbation data revealed that the backbones of S11 and R13 could participate in hydrogen-bonding interactions. Also, ring current shifts of the aromatic ring of F18 were apparent, attributable to hydrophobic interaction with Trm. As the S11 backbone is next to the disulfide bond C10−C27 and located outward of the loop region in all ensemble NMR structures of HBD (PDB 1KMX), this backbone cannot

dx.doi.org/10.1021/bi2000752 |*Biochemistry* 2011, 50, 4843–4854

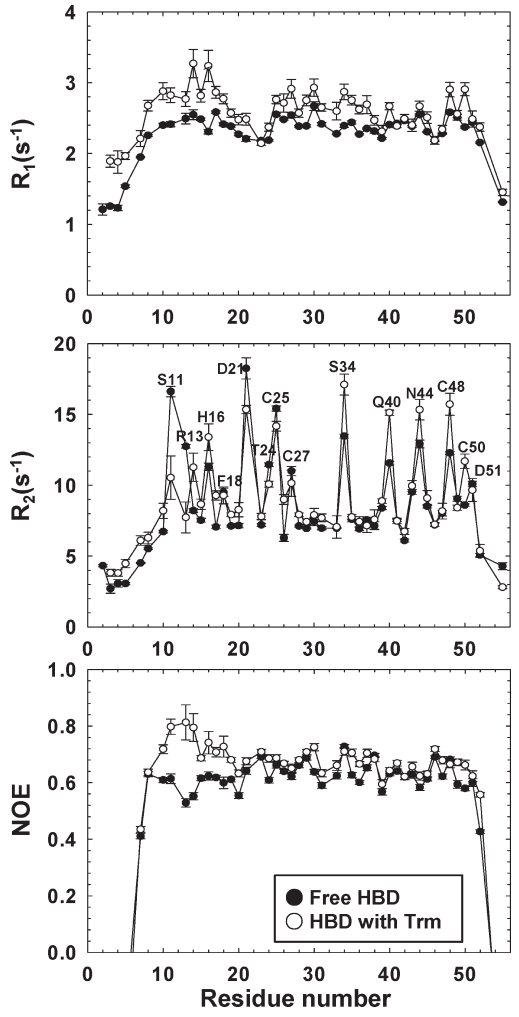

Figure 5. Comparison of R_1, R_2, and NOE values for free HBD (filled circles) and HBD complexed with Trm (open circles) at pH 5.5, at a molar ratio of HBD to Trm of 1:5. In the case of NOE data, N-terminal residues 1−5 and C-terminal residue 55 exhibited negative values.

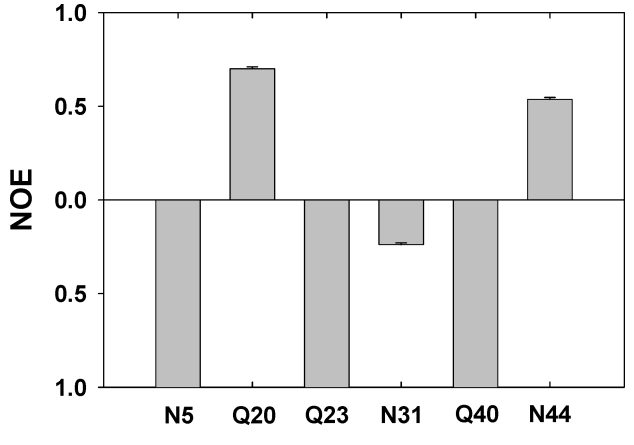

Figure 6. NOE values of side-chain amide resonances of asparagine and glutamine residues in the HBD.

directly form hydrogen bonds with Trm. To analyze the ring current shift of F18, we sought to apply distance constraints (2.5−5 Å) between the F18 ring center and the phenyl ring of

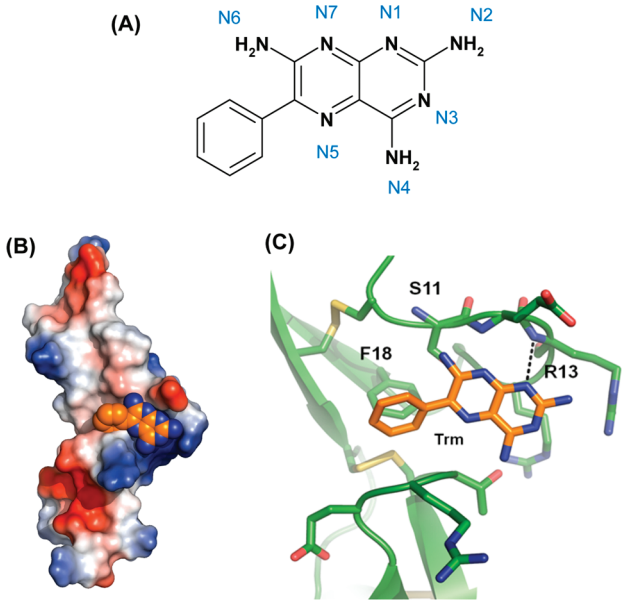

Figure 7. (A) 2D structure and numbering scheme of the Trm. (B) Overall structure of the HBD−Trm complex determined by docking studies. (C) Surface model illustrating the Trm bound to the N-terminal disordered loop region of the HBD. Binding model of the Trm and HBD showing hydrogen bond interaction (black dashed lines) involving backbone amide of R13 and hydrophobic interaction of the aromatic ring of F18 with Trm.

Trm, but steric hindrance was a major problem, with Trm being pushed away from the active site. Therefore, we applied a distance constraint to only the R13−Trm interaction. The docking model and the specific interactions involved are shown in Figure 7B,C. Trm and HBD interacted via one hydrogen bonds and one hydrophobic connection. The N1 atom of the pteridine ring formed a hydrogen bond with the backbone amide proton of R13. The phenyl ring of Trm participated in a hydrophobic interaction with the side-chain aromatic ring of F18. Docking induced a conformational change in comparison to the structure of free HBD, with a backbone rmsd of 0.209 Å. Notably, the loop region between S11 and F18 had a backbone rmsd of 0.491 Å, whereas the all-atom rmsd of this region was 0.675 Å. The S11 backbone was notably perturbed, with an rmsd of 1.367 Å. The backbones of R13 and F18 did not move to any great extent; the rmsd values were 0.134 and 0.124 Å, respectively. However, the side chains of these two residues moved through distances of 1.787 and 0.376 Å, respectively.

3.7. NMR-Derived Dynamics Parameters. Global and site-specific dynamics information for free HBD and Trm-bound HBD were obtained by model-free analysis, as described by Cole et al.[48] Using an axially symmetric diffusion tensor, we found that the rotational correlation time, τ_m, for free HBD and bound HBD were 5.34 ± 0.01 and 5.37 ± 0.02 ns, respectively, with corresponding $D_\parallel/D_\perp$ ratios of 1.38 and 1.25. Estimates of τ_m values suggested that binding of Trm does not cause HBD oligomerization.

We also determined the order parameter, S^2, describing the degree of spatial restriction of the backbone N−H bond vector by model-free analysis (Figure 8). The values of S^2 are colored onto the ribbon structure of HBD (1KMX[26]), and the values of R_{ex} for the residues are shown with a larger ribbon diameter in Figure 9. The average S^2 value of the HBD was 0.755 ± 0.013 and

dx.doi.org/10.1021/bi2000752 |*Biochemistry* 2011, 50, 4843–4854

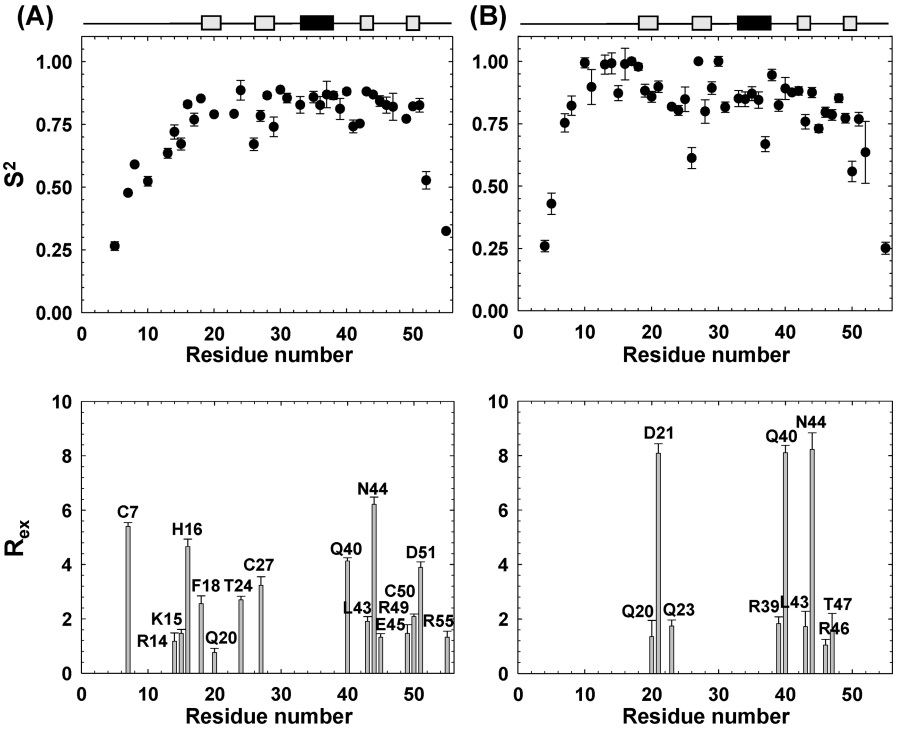

Figure 8. Optimized model-free parameters S^2 and R_{ex} for (A) free HBD and (B) HBD complexed with Trm at a molar ratio of HBD to Trm of 1:5. Secondary structure is shown above the data plot with rectangles indicating α-helical (black box) and β-sheet regions (gray box).

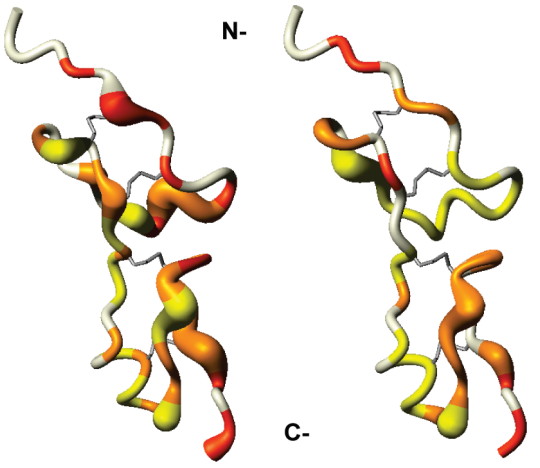

Figure 9. Spatial location of NMR-derived dynamics parameters of (A) free HBD and (B) HBD complexed with Trm. S^2 value-ranges are indicated in different colors in tubular drawings of (A) free HBD and (B) HBD complexed with Trm. Color scheme: yellow, $S^2 > 0.85$; orange, $0.65 < S^2 < 0.85$; dark orange, $S^2 < 0.65$. White indicates proline (6, 9, 22, and 53) and residues that were not included in model-free analysis. Residues with $R_{ex} > 0.5\ s^{-1}$ are shown with larger ribbon diameters. The figure was prepared using MolMol.[72]

that of the bound form was 0.810 ± 0.031, implying that binding of Trm renders the HBD more rigid by decreasing the overall internal motion.

The S^2 values for the residues near Trm-binding sites were most dramatically affected by Trm binding. For example, the S^2 value for R13 was increased from 0.615 ± 0.020 to 0.987 ± 0.038 and from 0.843 ± 0.009 to 0.978 ± 0.014 for F18. Unfortunately, S11 was not described by any model in free HBD. However, the S^2 value for that in bound form exhibited 0.897 ± 0.070 greater than average S^2 value (0.810 ± 0.031).

In the case of free HBD, most residues participating in secondary structure exhibited average S^2 values in the range of 0.780−0.860. The lowest S^2 value (0.615 ± 0.020) at the loop region of the N-terminus from S11 to F18 is consistent with the NOE values obtained in solution-NMR experiments. The lower time scale (microsecond−millisecond) motions were also captured from the model-free analysis. The values of R_{ex} greater than $0.5\ s^{-1}$ are shown in Figure 8. In free HBD, 11 residues at N- and C-terminal subdomains showed slow conformational motions ($R_{ex} > 2.0\ s^{-1}$). However, the slow motions of residues R14, K15, H16, and F18 at the N-terminal subdomain near the Trm binding site disappeared upon binding of Trm, whereas slow exchange at the C-terminal region persisted upon Trm binding. It appears that binding of Trm interfered with the slow conformational motions of the HBD at the N-terminal subdomain and resulted in structural stabilization of the HBD.

4. DISCUSSION AND CONCLUSIONS

VEGF plays a major role in angiogenesis and also has neurotrophic and neuroprotective effects. Structural studies of VEGF have been performed by a number of researchers. Muller et al. were the first to solve the 3D structure of VEGF, excluding the HBD in 1997 using X-ray crystallography.[58] The structure of the HBD of $VEGF_{165}$ was determined by Fairbrother et al. and Stauffer et al. using NMR spectroscopy.[25,26] VEGFs stimulate cellular responses by binding to tyrosine kinase receptors on the cell surface, such as the VEGF receptors Flt-1 (VEGFR-1) and KDR (VEGFR-2), members of the VEGF coreceptor family, and neuropilins. Extensive studies have revealed that complex structures are formed by these interactions between VEGFs and their

dx.doi.org/10.1021/bi2000752 |*Biochemistry* 2011, 50, 4843–4854

receptors.[59,60] Because the structural flexibility of the interface loop region (residues 11−17) is the reason for the poor defining of 3D structure of HBD, the structure of HBD is excluded in complex X-ray structure of VEGF and its receptors.[25] Inhibition of receptor activation by VEGF might have important therapeutic applications in diseases such as diabetic retinopathy and cancer. This potential has motivated the development of anti-VEGF antibodies and receptor-blocking peptides to suppress tumor growth and treat angiogenesis-related diseases.[61−65]

VEGF interacts with Aβ and accumulates in the senile plaques of AD patients' brains. This interaction has been proposed to lead to local deficiencies in available VEGF, giving rise to the hypothesis that the resulting loss of the protective effect of VEGF is responsible for, or contributes to, this neurodegenerative disorder.[6] It is known that Aβ binds to the HBD of $VEGF_{165}$ but not to the HBD of other growth factors,[5] implying that Aβ recognizes unique structural features of this $VEGF_{165}$ domain. In a previous study, we screened polypeptides and various other molecules, such as EGCG-like molecules, with the goal of identifying inhibitors capable of interacting with VEGF and blocking Aβ binding.[27] In particular, we sought inhibitors that interacted with the N-terminal side of the HBD of VEGF or, alternatively, with Aβ to disrupt VEGF−Aβ binding. These screens identified the inhibitor molecule Trm.[27] In the current study, we showed that Trm inhibits VEGF−Aβ interaction without affecting other biological activities of VEGF or Aβ. These results were confirmed by NMR experiments and docking studies, which showed that Trm binds to N-terminal loop region of the HBD.

In NMR experiments, the peaks corresponding to S11, R13, L17, and F18 showed large chemical shift perturbation (>0.1 ppm) in HSQC spectra. The signals on adding Trm to 0.4 mM HBD gradually shifted in one direction until the peaks of S11, R13, R14, and H16 were disappeared completely from the HSQC spectrum upon 4 mM of Trm added, indicating that Trm binds in a fast-weak binding pattern. The docking model described in section 3.6 showed that Trm and the HBD formed one hydrogen bond and one hydrophobic interaction. The N1 atom of the pteridine ring of Trm participated in hydrogen-bonding interaction with backbone amide proton of R13. The phenyl ring of Trm and the aromatic ring of F18 formed a hydrophobic interaction at the proposed Trm binding site. This hydrogen bond and one hydrophobic interaction contributed to the binding of Trm to the HBD. Thus, the results of NMR experiments were well explained by the docking model, and these interactions provide important information about further development of more potent inhibitors of VEGF−Aβ interactions.

Heparin, which has a very high negative-charge density, has regulatory effects on the binding of VEGF to its receptor. Heparin-binding sites take the form of a positively charged pocket and are commonly located on the surface of proteins.[22,66] It is known that the site within the HBD of $VEGF_{165}$ that binds heparin is composed of R13, R14, and R49, whose side chains form stable electrostatic interactions with heparin.[22,66] This site is located on the opposite side of our proposed Trm binding site in the HBD. Our docking and chemical shift perturbation results showed that the backbone amide of R13 forms a hydrogen bond with Trm while R14 as well as K15 showed little chemical shift perturbation upon binding with Trm. Therefore, heparin binding to the side chain of R14 in the HBD cannot be affected by Trm binding. In this work, we confirmed that Trm binding to the HBD did not affect interaction of VEGF with KDR, implying that Trm binding to the HBD does not affect heparin binding, either. This suggests that R13 is much less critical for heparin binding than are the residues R14 and R49; this interpretation has been confirmed by mutagenesis experiments.[22,66] These latter studies, which examined the heparin-binding activity of various $VEGF_{164}$ HBD mutants containing substitutions at positively charged residues in the vicinity of the heparin-binding site, showed that the R13A/R14A/R49A triple mutant significantly affected heparin binding, dramatically increasing the dissociation constant. The dissociation constant was also substantially increased in the R14A/R49A double mutant. Collectively, these data argue that the side chains of R13, R14, and R49 constitute a potential heparin-binding surface of the HBD and that residues R14 and R49 are the critical heparin-binding residues.[66]

The dynamics of protein molecules is a critical aspect of their biophysical properties and biological functions, playing an important role in enzyme catalysis, conformational rearrangement, ligand binding, and molecular-recognition processes.[29−32,67−69] Biological events occur on widely divergent time scales, ranging from picoseconds to seconds, and solution-NMR spin-relaxation techniques have emerged as a powerful tool for studying internal protein dynamics. Here, we analyzed the dynamics of free HBD and HBD−Trm complexes and investigated the roles of HBD motional properties in HBD function. The 3D structure of the HBD in $VEGF_{165}$ was determined previously by Fairbrother and co-workers,[25] who were also the first to recognize the dynamics of this domain. Their analysis revealed the presence of highly mobile residues in the N-terminus (including a disordered loop region corresponding to residues 11−17) and C-terminus based on steady-state $^1H-^{15}N$ NOE data. In a subsequent study, the subdomain orientations of the HBD were improved using residual dipolar coupling constraints.[26] In the current study, we analyzed spin-relaxation data to provide a detailed view of free HBD and HBD complexed with Trm. The results revealed that the HBD is highly mobile, with chemical exchange of the disordered loop region at the N-terminal subdomain that occur over micro- and millisecond time frames being critical for interactions with Trm.

As expected, our analysis showed that residues at N- and C-termini, which have very low NOE values, appear to undergo rapid (nanopicosecond) internal dynamics. In accordance with these data, generalized order parameters in these regions were low (Figure 8). It is well-known that N-terminal residues (1−6) are recognized by plasmin for cleavage whereas positively charged residues in the C-terminal subdomain (K30, R35, R39, R46, and R49) are recognized by heparin.[66] We expect that the flexibility of the HBD of VEGF is critical for interactions with other proteins necessary to transduce cell signals. Residues that undergo slow time scale motion are spread throughout the protein, as shown in Figure 8. Most exhibit high R_{ex} values, possibly due to loop motion, *cis*−*trans*-proline isomerization, or disulfide bond isomerization.[70,71] The HBD contains four proline residues (6, 9, 22, and 53) and four disulfide bonds (7−25, 10−27, 29−48, and 36−50). Interestingly, the S^2 value of the ss-strand-forming K26 residue was less than 0.7 and was significantly lower than that of other ordered regions, implying disulfide bond isomerization of C25 and C27. The Q40, L43, N44, E45, R49, and D51 residues, which exhibited chemical exchange (Figure 8A), are located near positively charged C-terminal residues K37, R39, R46, R49, and K52, which are involved in heparin binding.[66]

We expect that molecular motions in the HBD that are important for recognition of heparin or other proteins contribute

to the function of VEGF. Notably, residues in the disordered loop region of the N-terminus exhibited conformational exchanges including R14, K15, H16, and F18 in free HBD that are important for Trm binding. Average NOE and S^2 values of this loop region showed great flexibility in free HBD but became more rigid upon binding Trm. Notably, Trm binding was associated with increased rigidity and the disappearance of chemical exchanges for residues near the Trm binding site. In contrast, C-terminal residues continued to exhibit slow conformational motions, even in the HBD−Trm complex. Therefore, binding of Trm appears to stabilize the N-terminal subdomain, but not the C-terminal subdomain. Because the experimental data in this study showed that Trm did not inhibit the interaction between $VEGF_{165}$ and its receptor KDR, the Trm binding site is different from that of heparin. It can further be suggested that slow time scale motions at the C-terminus of the HBD might be important for interactions with heparin molecules. These motions on a slow time scale can participate directly in ligand−protein-recognition processes. In this study, it was successfully shown that disordered N-terminal loop region of HBD plays an important role in molecular-recognition processes. Furthermore, Aβ may recognize these structural flexibilities as well as the unique structural features of the HBD of $VEGF_{165}$. The flexibility of HBD demonstrated here should be essential for VEGF function and interaction with other protein partners. Based on the results obtained here, more potent inhibitors of VEGF−Aβ interaction which does not disturb the heparin binding to the C-terminus but recognizes the flexible N-terminal loop region can be developed as a therapeutic agent for Alzheimer's disease.

AUTHOR INFORMATION

Corresponding Author

*Tel: 82-2-450-3421. Fax: 82-2-447-5987. E-mail: ymkim@konkuk.ac.kr.

Funding Sources

This work was supported by National Research Foundation of Korea (NRF) funded by the Ministry of Education, Science and Technology (2009-0076064) and by Priority Research Centers Program through the National Research Foundation of Korea (NRF) funded by the Ministry of Education, Science and Technology (2009-0093824). This study made use of the NMR facility at the Korea Basic Science Institute, which is supported by the Bio-MR research program of the Korean Ministry of Science and Technology (E28070).

ABBREVIATIONS

Aβ, β-amyloid; AD, Alzheimer's disease; EGCG, epigallocatechin gallate; HBD, heparin-binding domain; HSQC, heteronuclear single-quantum coherence; MD, molecular dynamics; NMR, nuclear magnetic resonance; NOE, nuclear Overhauser effect; Trm, triamterene; VEGF, vascular endothelial growth factor.

REFERENCES

(1) Yankner, B. A. (1996) Mechanisms of neuronal degeneration in Alzheimer's disease. *Neuron 16*, 921–932.

(2) Hardy, J., and Selkoe, D. J. (2002) The amyloid hypothesis of Alzheimer's disease: progress and problems on the road to therapeutics. *Science 297*, 353–356.

(3) Sommer, B. (2002) Alzheimer's disease and the amyloid cascade hypothesis: 10 years on. *Curr. Opin. Pharmacol. 2*, 87–92.

(4) Yang, S.-P., Bae, D.-G., Kang, H. J., Gwag, B. J., Gho, Y. S., and Chae, C.-B. (2004) Co-accumulation of vascular endothelial growth factor with β-amyloid in the brain of patients with Alzheimer's disease. *Neurobiol. Aging 25*, 283–290.

(5) Yang, S.-P., Kwon, B. O., Cho, Y. S., and Chae, C.-B. (2005) Specific interaction of VEGF165 with β-amyloid, and its protective effect on β-amyloid-induced neurotoxicity. *J. Neurochem. 93*, 118–127.

(6) Dvorak, H. F., Brown, L. F., Detmar, M., and Dvorak, A. M. (1995) Vascular permeability factor/vascular endothelial growth factor, microvascular hyperpermeability, and angiogenesis. *Am. J. Pathol. 146*, 1029–1039.

(7) Ferrara, N. (1995) The role of vascular endothelial growth factor in pathological angiogenesis. *Breast Cancer Res. Treat. 36*, 127–137.

(8) Carmeliet, P., Ferreira, V., Breier, G., Pollefeyt, S., Kieckens, L., Gertsenstein, M., Fahrig, M., Vandenhoeck, A., Harpal, K., Eberhardt, C., Declercq, C., Pawling, J., Moons, L., Collen, D., Risau, W., and Nagy, A. (1996) Abnormal blood vessel development and lethality in embryos lacking a single VEGF allele. *Nature 380*, 435–439.

(9) Ferrara, N., Carver-Moore, K., Chen, H., Dowd, M., Lu, L., O'Shea, K. S., Powell-Braxton, L., Hillan, K. J., and Moore, M. W. (1996) Heterozygous embryonic lethality induced by targeted inactivation of the VEGF gene. *Nature 380*, 439–442.

(10) Folkman, J. (1995) Angiogenesis in cancer, vascular, rheumatoid and other disease. *Nature Med. 1*, 27–31.

(11) Jin, K. L., Mao, X. O., and Greenberg, D. A. (2000) Vascular endothelial growth factor rescues HN33 neural cells from death induced by serum withdrawal. *J. Mol. Neurosci. 14*, 197–203.

(12) Jin, K. L., Mao, X. O., and Greenberg, D. A. (2000) Vascular endothelial growth factor: direct neuroprotective effect in in vitro ischemia. *Proc. Natl. Acad. Sci. U.S.A. 97*, 10242–10247.

(13) Storkebaum, E., and Carmeliet, P. (2004) VEGF: a critical player in neurogeneration. *J. Cin. Invest. 113*, 14–18.

(14) Muller, Y. A., Christinger, H. W., Keyt, B. A., and de Vos, A. M. (1997) The crystal structure of vascular endothelial growth factor (VEGF) refined to 1.93 Å resolution: multiple copy flexibility and receptor binding. *Structure 5*, 1325–1338.

(15) Sun, P. D., and Davies, D. R. (1995) The cystine-knot growth-factor superfamily. *Annu. Rev. Biophys. Biomol. Struct. 24*, 269–291.

(16) McDonald, N. Q., and Hendrickson, W. A. (1993) A structural superfamily of growth factors containing a cystine knot motif. *Cell 73*, 421–424.

(17) Murray-Rust, J., McDonald, N. Q., Blundell, T. L., Hosang, M., Oefner, C., Winkler, F., and Bradshaw, R. A. (1993) Topological similarities in TGF-β2, PDGF-BB and NGF define a superfamily of polypeptide growth factors. *Structure 1*, 153–159.

(18) Isaacs, N. W. (1995) Cystine knots. *Curr. Opin. Struct. Biol. 5*, 391–395.

(19) Ferrara, N. (2009) Vascular endothelial growth factor: Basic biology and clinical applications. *Curr. Clin. Onco. 1*, 11–21.

(20) Hoeben, A., Landuyt, B., Highley, M. S., Wildiers, H., Van Oosterom, A. T., and De Bruijn, E. A. (2004) Vascular endothelial growth factor and angiogenesis. *Pharmacol. Rev. 56*, 549–580.

(21) Keyt, B. A., Berleau, L. T., Nguyen, H. V., Chen, H., Heinsohn, H., Vandlen, R., and Ferrara, N. (1996) The carboxyl-terminal domain (111−165) of vascular endothelial growth factor is critical for its mitogenic potency. *J. Biol. Chem. 271*, 7788–7795.

(22) Krilleke, D., Ng, Y. S., and Shima, D. T. (2009) The heparin-binding domain confers diverse functions of VEGF-A in development and disease: a structure-function study. *Biochem. Soc. Trans. 37*, 1201–1206.

(23) Ashikari-Hada, S., Habuchi, H., Kariya, Y., and Kimata, K. (2005) Heparin regulates vascular endothelial growth factor165-dependent mitogenic activity, tube formation, and its receptor phosphorylation of human endothelial cells. Comparison of the effects of heparin and modified heparins. *J. Biol. Chem. 280*, 31508–31515.

(24) Hamma-Kourbali, Y., Vassy, R., Starzec, A., Le Meuth-Metzinger, V., Oudar, O., Bagheri-Yarmand, R., Perret, G., and Crépin, M. (2001) Vascular endothelial growth factor 165 ($VEGF_{165}$) activities are inhibited by carboxymethyl benzylamide dextran that competes for

heparin binding to $VEGF_{165}$ and $VEGF_{165}$.KDR complexes. *J. Biol. Chem. 276*, 39748–39754.

(25) Fairbrother, W. J., Champe, M. A., Christinger, H. W., Keyt, B. A., and Starovasnik, M. A. (1998) Solution structure of the heparin-binding domain of vascular endothelial growth factor. *Structure 15*, 637–648.

(26) Stauffer, M. E., Skelton, N. J., and Fairbrother, W. J. (2002) Refinement of the solution structure of the heparin binding domain of vascular endothelial growth using residual dipolar coupling. *J. Biomol. NMR 23*, 57–61.

(27) Chae, C. B., Gho, Y. S., Yang, S., Bae, D. G., Kwon, B. O., and Hwang, S. (2010) Methods of Contacting β amyloid protein with VEGF, U.S. Patent 7,795,213 B2.

(28) Mukne, A. P., and Nagarsenker, M. S. (2004) Triamterene-β-cyclodextrin systems: preparation, characterization and in vivo evaluation. *AAPS Pharm. Sci. Tech. 5*, 142–150.

(29) Eisenmesser, E. Z., Bosco, D. A., Akke, M., and Kern, D. (2002) Enzyme dynamics during catalysis. *Science 295*, 1520–1523.

(30) Venkitakrishnan, R. P., Zaborowski, E., McElheny, D., Benkovic, S. J., Dyson, H. J., and Wright, P. E. (2004) Conformational changes in the active site loops of dihydrofolate reductase during the catalytic cycle. *Biochemistry 43*, 16046–16055.

(31) Cole, R., and Loria, J. P. (2002) Evidence for flexibility in the function of ribonuclease A. *Biochemistry 41*, 6072–6081.

(32) Codreanu, S. G., Ladner, J. E., Xiao, G. Y., Stourman, N. V., Hachey, D. L., Gilliland, G. L., and Armstrong, R. N. (2002) Local protein dynamics and catalysis: Detection of segmental motion associated with rate-limiting product release by a glutathione transferase. *Biochemistry 41*, 15161–15172.

(33) Bae, D.-G., Gho, Y.-S., Yoon, W.-H., and Chae, C.-B. (2000) Arginine-rich anti-vascular endothelial growth factor peptides inhibit tumor growth and metastasis by blocking angiogenesis. *J. Biol. Chem. 275*, 13588–13596.

(34) Bae, D.-G., Kim, T. D., Li, G., Yoon, W.-H., and Chae, C.-B. (2005) Anti-Flt1 peptide, a vascular endothelial growth factor receptor 1- Specific hexapeptide, inhibits tumor growth and metastasis. *Clin. Cancer Res. 11*, 2651–2661.

(35) Levine, H., III (1993) Thioflavine T interaction with synthetic Alzheimer's disease beta-amyloid peptides: detection of amyloid aggregation in solution. *Protein Sci. 2* (3), 404–410.

(36) Goodsell, D. S., Morris, G. M., and Olson, A. J. (1996) Automated docking of flexible ligands: applications of AutoDock. *J. Mol. Recognit. 9* (1), 1–5.

(37) Morris, G. M., Goodsell, D. S., Halliday, R. S., Huey, R., Hart, W. E., Belew, R. K., and Olson, A. J. (1998) Automated docking using a Lamarckian genetic algorithm and an empirical binding free energy function. *J. Comput. Chem. 19*, 1639–1662.

(38) Marion, E., Driscoll, P. C., Kay, L. E., Wingfield, P. T., Bax, A., Gronenborn, A. M., and Clore, G. M. (1989) Overcoming the overlap problem in the assignment of 1H NMR spectra of larger proteins by use of three dimensional heteronuclear 1H-15N Hartmann−Hahn-multiple quantum coherence and nuclear overhauser-multiple quantum coherence spectroscopy: application to interleukin 1 beta. *Biochemistry 28*, 6150–6156.

(39) Cavanagh, J., and Rance, M. (1990) Sensitivity improvement in isotropic mixing (TOCSY) experiments. *J. Magn. Reson. 88*, 72–85.

(40) Kordel, J., Skelton, N. J., Akke, M., Plamer, A. G., III, and Chazin, W. J. (1992) Backbone dynamics of calcium-loaded calbindin D9k studied by two dimensional proton-detected 15N NMR spectroscopy. *Biochemistry 31*, 4856–4866.

(41) Skelton, N. J., Palmer, A. G., III, Akke, M., Kördel, J., Rance, M., and Chazin, W. J. (1993) Practical aspects of two-dimensional proton-detected 15N spin relaxation measurements. *J. Magn. Reson., Ser. B 102*, 253–264.

(42) Kay, L. E., Keifer, P., and Saarinen, T. (1992) Pure absorption gradient enhanced heteronuclear single quantum correlation spectroscopy with improved sensitivity. *J. Am. Chem. Soc. 114*, 10663–10665.

(43) Kempf, J. G., and Loria, J. P. (2003) in *Protein NMR Techniques* (Downing, A. K., Ed.) Humana Press, Totowa.

(44) Delaglio, F., Grzesiak, S., Vuister, G. W., Zhu, G., Pfeifer, J., and Bax, A. (1995) NMRPipe: a multidimensional spectral processing system based on UNIX pipes. *J. Biomol. NMR 6*, 277–293.

(45) Goddard, T. D., and Kneller, D. G. SPARKY 3, University of California, San Francisco.

(46) Lipari, G., and Szabo, A. (1982) Model-free approach to the interpretation of nuclear magnetic resonance relaxation in macromolecules. 1. Theory and range of validity. *J. Am. Chem. Soc. 104*, 4546–4559.

(47) Lipari, G., and Szabo, A. (1982) Model-free approach to the interpretation of nuclear magnetic resonance relaxation in macromolecules. 2. Analysis of experimental results. *J. Am. Chem. Soc. 104*, 4559–4570.

(48) Cole, R., and Loria, J. P. (2003) Fast-modelfree: a program for rapid automated analysis of solution NMR spin-relaxation data. *J. Biomol. NMR 26*, 203–213.

(49) Clore, G. M., Szabo, A., Bax, A., Kay, L. E., Driscoll, P. C., and Gronenborn, A. M. (1990) Deviations from the simple two-parameter model-free approach to the interpretation of 15N nuclear magnetic relaxation of proteins. *J. Am. Chem. Soc. 112*, 4989–4991.

(50) Palmer, A. G., III, Rance, M., and Wright, P. E. (1991) Intramolecular motions of a zinc finger DNA-binding domain from Xfin characterized by proton detected natural abundance 13C heteronuclear NMR spectroscopy. *J. Am. Chem. Soc. 113*, 4371–4380.

(51) Mandel, A. M., Akke, M., and Palmer, A. G., III (1995) Backbone dynamics of *Escherichia coli* ribonuclease HI: correlations with structure and function in an active enzyme. *J. Mol. Biol. 246*, 144–163.

(52) Tjandra, N., Feller, S. E., Pastor, R. W., and Bax, A. (1995) Rotational diffusion anisotropy of human ubiquitin from 15N NMR relaxation. *J. Am. Chem. Soc. 117*, 12562–12566.

(53) Hiyama, Y., Niu, C.-H., Silverton, J. V., Bavoso, A., and Torchia, D. A. (1988) Determination of 15N chemical shift tensor via 15N−2H dipolar coupling in Boc-glycylglycyl [15N glycine] benzyl ester. *J. Am. Chem. Soc. 110*, 2378–2383.

(54) Fairbrother, W. J., Liu, J., Pisacane, P. I., Sliwkowski, M. X., and Palmer, A. G., III (1998) Backbone dynamics of the EGF-like domain of heregulinalpha. *J. Mol. Biol. 279*, 1149–1161.

(55) Lamy, S., Gingras, D., and Beliveau, R. (2002) Green tea catechins inhibit vascular endothelial growth factor receptor phosphorylation. *Cancer Res. 62*, 381–385.

(56) Kondo, T., Ohta, T., Igura, K., Hara, Y., and Kaji, K. (2002) Tea catechins inhibit angiogenesis in vitro, measured by human endothelial cell growth, migration and tube formation, through inhibition of VEGF receptor binding. *Cancer Lett. 180*, 139–144.

(57) Pellecchia, M., Sebbel, P., Hermanns, U., Wuthrich, K., and Glockshuber, R. (1999) Pilus chaperone FimC−adhesin FimH interactions mapped by TROSY-NMR. *Nat. Struct. Biol. 6*, 336–339.

(58) Muller, Y. A., Li, B., Christinger, H. W., Wells, J. A., Cunningham, B. C., and de Vos, A. M. (1997) Vascular endothelial growth factor: crystal structure and functional mapping of the kinase domain receptor binding site. *Proc. Natl. Acad. Sci. U.S.A. 94*, 7192–7197.

(59) Starovasnik, M. A., Christinger, H. W., Wiesmann, C., Champe, M. A., de Vos, A. M., and Skelton, N. J. (1999) Solution structure of the VEGF-binding domain of Flt-1: comparison of its free and bound states. *J. Mol. Biol. 293*, 531–544.

(60) Iyer, S., Darley, P. I., and Acharya, K. R. (2010) Structural insights into the binding of vascular endothelial growth factor-B by VEGFR-1(D2): recognition and specificity. *J. Biol. Chem. 285*, 23779–23789.

(61) Muller, Y. A., Chen, Y., Christinger, H. W., Li, B., Cunningham, B. C., Lowman, H. B., and de Vos, A. M. (1998) VEGF and the Fab fragment of a humanized neutralizing antibody: crystal structure of the complex at 2.4 A resolution and mutational analysis of the interface. *Structure 6*, 1153–1167.

(62) Wiesmann, C., Christinger, H. W., Cochran, A. G., Cunningham, B. C., Fairbrother, W. J., Keenan, C. J., Meng, G., and de Vos, A. M. (1998) Crystal structure of the complex between VEGF and a receptor-blocking peptide. *Biochemistry 37*, 17765–17772.

(63) Chen, Y., Wiesmann, C., Fuh, G., Li, B., Christinger, H. W., McKay, P., de Vos, A. M., and Lowman, H. B. (1999) Selection and analysis of an optimized anti-VEGF antibody: crystal structure of an affinity-matured Fab in complex with antigen. *J. Mol. Biol. 293*, 865–881.

(64) Appleton, B. A., Wu, P., Maloney, J., Yin, J., Liang, W. C., Stawicki, S., Mortara, K., Bowman, K. K., Elliott, J. M., Desmarais, W., Bazan, J. F., Bagri, A., Tessier-Lavigne, M., Koch, A. W., Wu, Y., Watts, R. J., and Wiesmann, C. (2007) Structural studies of neuropilin/antibody complexes provide insights into semaphorin and VEGF binding. *EMBO J. 26*, 4902–4912.

(65) Leonard, P., Scotney, P. D., Jabeen, T., Iyer, S., Fabri, L. J., Nash, A. D., and Acharya, K. R. (2008) Crystal structure of vascular endothelial growth factor-B in complex with a neutralising antibody Fab fragment. *J. Mol. Biol. 384*, 1203–1217.

(66) Krilleke, D., DeErkenez, A., Schubert, W., Giri, I., Robinson, G. S., Ng, Y. S., and Shima, D. T. (2007) Molecular mapping and functional characterization of the VEGF164 heparin-binding domain. *J. Biol. Chem. 282*, 28045–28056.

(67) Long, D., and Yang, D. (2010) Millisecond timescale dynamics of human liver fatty acid binding protein: testing of its relevance to the ligand entry process. *Biopys. J. 98* (12), 3054–53061.

(68) Baldwin, A. J., and Kay, L. E. (2009) NMR spectroscopy brings invisible protein states into focus. *Nat. Chem. Biol. 5* (11), 808–814.

(69) Loria, J. P., Berlow, R. B., and Watt, E. D. (2008) Characterization of enzyme motions by solution NMR relaxation dispersion. *Acc. Chem. Res. 41* (2), 214–221.

(70) Grey, M. J., Wang, C., and Palmer, A. G., III (2003) Disulfide bond isomerization in basic pancreatic trypsin inhibitor: Multisite chemical exchange quantified by CPMG relaxation dispersion and chemical shift modeling. *J. Am. Chem. Soc. 125*, 14324–14335.

(71) Chi, Y. H., Kumar, T. K. S., Chiu, I. M., and Yu, C. (2000) ^{15}N NMR relaxation studies of free and ligand-bound human acidic fibroblast growth factor. *J. Biol. Chem. 275*, 39444–39450.

(72) Koradi, R., Billeter, M., and Wuthrich, K. (1996) MOLMOL: a program for display and analysis of macromolecular structures. *J. Mol. Graphics 14*, 51–55.